

Single-photon quantum regime of artificial radiation pressure on a surface acoustic wave resonator

Atsushi Noguchi^{1,2,*}, Rekishu Yamazaki¹, Yutaka Tabuchi¹, and Yasunobu Nakamura^{1,3}

¹*Research Center for Advanced Science and Technology (RCAST),*

The University of Tokyo, Meguro-ku, Tokyo, 153-8904, Japan,

²*PRESTO, Japan Science and Technology Agency, Kawaguchi-shi, Saitama 332-0012, Japan,*

³*Center for Emergent Matter Science (CEMS), RIKEN, Wako-shi, Saitama 351-0198, Japan*

(Dated: May 28, 2022)

PACS numbers:

Electromagnetic fields carry momentum, which upon reflection on matter, gives rise to the radiation pressure of photons [1]. The radiation pressure has recently been utilized in cavity optomechanics for controlling mechanical motions of macroscopic objects at the quantum limit [2]. However, because of the weakness of the interaction, attempts so far had to use a strong coherent drive to reach the quantum limit [3–8]. Therefore, the single photon quantum regime, where even the presence of a totally off-resonant single photon alters the quantum state of the mechanical mode significantly, is one of the next milestones in cavity optomechanics [2]. Here we demonstrate an artificial realization of the radiation pressure of microwave photons acting on phonons in a surface acoustic wave resonator. The order-of-magnitude enhancement of the interaction strength originates in the well-tailored strong second-order nonlinearity of a superconducting Josephson-junction circuit [9]. The synthetic radiation pressure interaction adds a key element to the quantum optomechanical toolbox and can be applied to quantum information interfaces between electromagnetic and mechanical degrees of freedom.

The radiation pressure is one of the fundamental concepts in cavity optomechanics [2]. It arises from the frequency shift of the optical (or electrical) resonator depending on the displacement of the mechanical system. The associated interaction energy is proportional to the acoustic field amplitude and to the square of the electromagnetic field amplitude. This second-order nonlinearity is the essential feature of the radiation pressure interaction. Even though the interaction is rather weak at the single-photon level, one can apply a strong drive field to enhance the effective coupling strength to reach the quantum regime [3, 6]. Based on this interaction, ground-state cooling and quantum state control of mechanical oscillators have been reported on suspended membranes [3–5], phononic crystal cavities [6–8], microtoroidal resonators [10], and bulk oscillators [11].

The single-photon quantum regime is reached when the radiation pressure is strong enough to overcome other

dissipations in the system [2], where the quantum state of the mechanical mode is coherently controlled by the quantum electromagnetic field. However, such a strong radiation pressure interaction has been elusive in optomechanical systems studied so far, though there are a few experiments approaching this regime [12, 13].

Recently, surface acoustic waves (SAW) have attracted much interest as an alternative quantum acoustic mode localized at the surface of a substrate [14, 15]. In piezoelectric materials, SAW strongly couple to electric fields between surface electrodes. Their low-loss and small-wavelength features have been commercially applied to compact high-frequency components such as filters and sensors [16]. In the quantum limit, the small mode volume of a SAW resonator also enhances the coupling strength between photons and phonons. Hybrid systems with a superconducting qubit were recently demonstrated [17–21], where the Jaynes-Cummings-type interaction between the superconducting qubit and the SAW resonator phonons was used. However, a nonlinear interaction, such as the radiation pressure interaction, has not been implemented in those systems.

To achieve the single-photon quantum regime with a radiation pressure interaction, we introduce an artificial optomechanical system consisting of a SAW resonator and a superconducting circuit. Superconducting circuits with Josephson junctions are known to be a versatile platform to engineer a strong nonlinearity with negligible dissipation [9, 22–24]. Here we exploit the nonlinearity of Josephson junctions and synthesize a strong second-order nonlinearity in the hybrid system.

Our hybrid system is composed of a Fabry-Pérot-type SAW resonator, defined by a pair of Bragg mirrors, and a nonlinear microwave (MW) resonator (Fig. 1a). They are coupled to each other via an interdigitated transducer (IDT) through the piezoelectric interaction. All the structures are made of aluminum evaporated on a ST-X quartz substrate (See the details in the Supplementary Information [25]).

The nonlinear MW resonator consists of a short coplanar waveguide connected to the IDT on one end. On the other end it is grounded via a loop interrupted by one small and two large Josephson junctions with the Josephson energies E'_J and E_J , respectively. The circuit

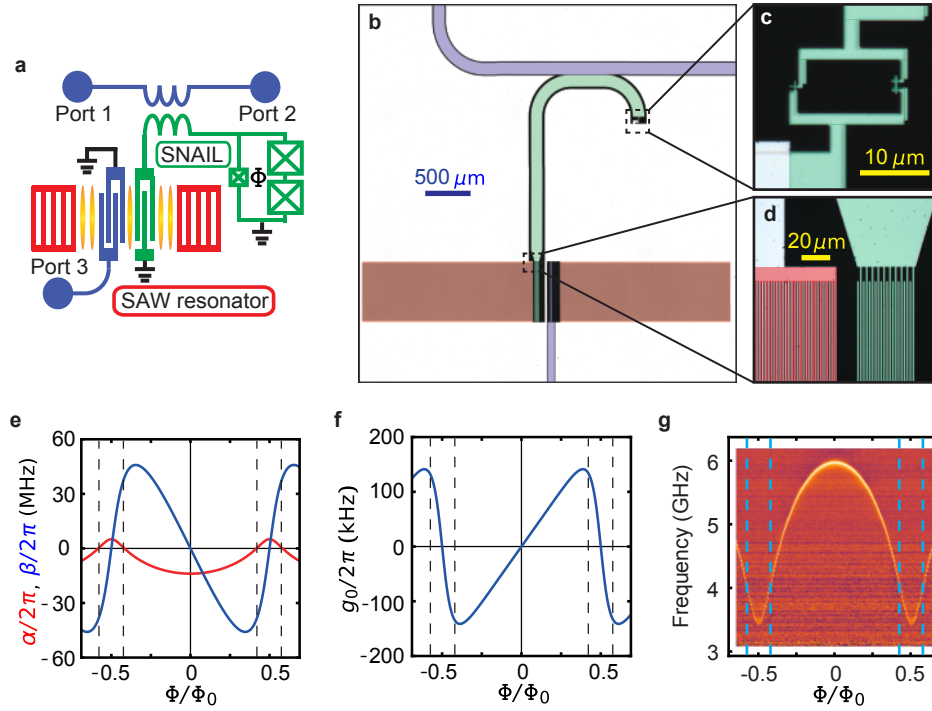


FIG. 1: **SAW-MW hybrid system for artificial radiation pressure interaction.** **a.** Schematic of the SAW optomechanical system. A SAW resonator defined by Bragg mirrors (red) couples to a nonlinear MW resonator (green) via an interdigitated transducer. A SNAIL loop consisting of three Josephson junctions works as a nonlinear inductive element. Ports 1 and 2 are external feed lines for the MW resonator, and port 3 is that for the SAW resonator having a spatial mode shown in yellow. **b-d.** False-colored micrographs of the sample. The colors of the electrodes correspond to the ones in the schematic in **a.** **c.** Magnification of the SNAIL part. The three junctions form the SNAIL loop. **d.** Zoom-up of a part of the SAW resonator and the interdigitated transducer. **e.** Calculated nonlinearity of the MW resonator as a function of the magnetic flux Φ penetrating through the SNAIL loop. Blue (red) curve represents the self-Kerr (Pockels) nonlinearity α (β) of the MW resonator. **f.** Calculated strength g_0 of the artificial radiation pressure interaction induced by the nonlinearity of the SNAIL. **g.** Spectrum of the nonlinear resonator as a function of Φ measured with a weak MW probe whose average intra-resonator photon number is much less than unity. Vertical dashed lines in **e-g** indicate flux bias conditions where the self-Kerr nonlinearity vanishes in numerical simulations.

element is called the Superconducting Nonlinear Asymmetric Inductive eLement (SNAIL) [9]. The SNAIL has the inductive energy

$$U(\theta) = -E'_J \cos \theta - 2E_J \cos \left(\frac{\phi - \theta}{2} \right), \quad (1)$$

where θ is the superconducting phase across the small junction, $\phi = 2\pi\Phi/\Phi_0$ is the reduced magnetic flux, Φ is the flux threading the loop, and $\Phi_0 = h/2e$ is the flux quantum. The SNAIL capacitively shunted with the coplanar waveguide forms the nonlinear MW resonator, whose Hamiltonian reads (with $\hbar = 1$)

$$\hat{H}_m = \omega_m \hat{a}^\dagger \hat{a} + \alpha_0 \hat{a}^\dagger \hat{a}^\dagger \hat{a} \hat{a} + \beta (\hat{a}^\dagger \hat{a}^\dagger \hat{a} + \text{h.c.}). \quad (2)$$

Here \hat{a} (\hat{a}^\dagger) is the annihilation (creation) operator of a photon in the MW resonator, and ω_m is the resonance frequency. The terms with coefficients α_0 and β represent the nonlinearities of the resonator corresponding to the self-Kerr and Pockels effects, respectively.

The Hamiltonian of the hybrid system consisting of the MW and SAW resonators is written as

$$\hat{H} = \hat{H}_0 + \hat{V}, \quad (3)$$

where

$$\hat{H}_0 = \omega_m \hat{a}^\dagger \hat{a} + \omega_s \hat{b}^\dagger \hat{b}, \quad (4)$$

and

$$\hat{V} = \alpha_0 \hat{a}^\dagger \hat{a}^\dagger \hat{a} \hat{a} + \beta (\hat{a}^\dagger \hat{a}^\dagger \hat{a} + \text{h.c.}) + g (\hat{a}^\dagger \hat{b} + \hat{a} \hat{b}^\dagger). \quad (5)$$

Here \hat{b} (\hat{b}^\dagger) is the annihilation (creation) operator of a phonon in the SAW resonator, ω_s is the resonance frequency, and g is the piezoelectric coupling strength between the SAW and MW resonators. By treating \hat{V} as a perturbation (See the details in the Supplementary Information [25]), we obtain the effective interaction Hamil-

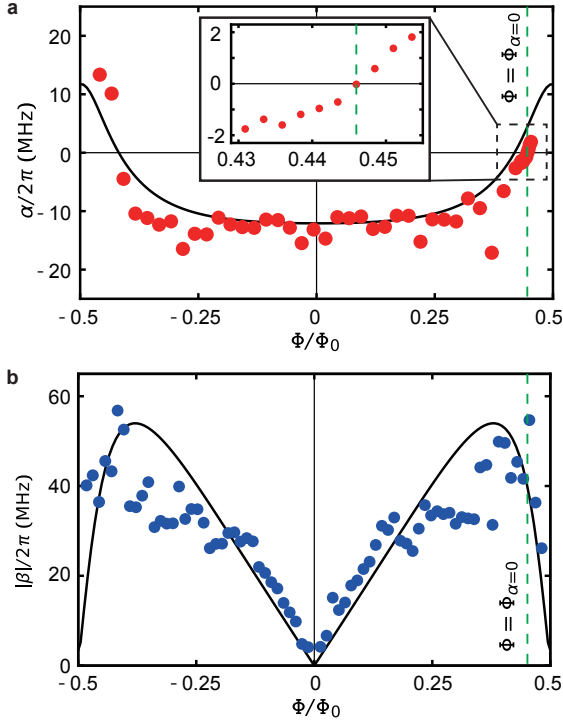


FIG. 2: **Nonlinearity of the MW resonator.** **a.** Self-Kerr nonlinearity α as a function of the flux through the SNAIL loop. Inset shows the enlarged view around $\Phi = \Phi_{\alpha=0}$. **b.** Absolute value of the Pockels nonlinearity $|\beta|$ as a function of the magnetic flux bias. The curve in each panel shows the result of the numerical simulation without any fitting parameters. Green dashed lines indicate $\Phi = 0.445\Phi_0 = \Phi_{\alpha=0}$.

tonian

$$\begin{aligned} \hat{V}_{\text{eff}} &= \left(\alpha_0 - \frac{3\beta^2}{\omega_m} \right) \hat{a}^\dagger \hat{a}^\dagger \hat{a} \hat{a} - \left(\frac{2g\beta}{\omega_m - \omega_s} \right) \hat{a}^\dagger \hat{a} (\hat{b}^\dagger + \hat{b}), \\ &\equiv \alpha \hat{a}^\dagger \hat{a}^\dagger \hat{a} \hat{a} + g_0 \hat{a}^\dagger \hat{a} (\hat{b}^\dagger + \hat{b}), \end{aligned} \quad (6)$$

under the rotating-wave approximation. This derivation is valid when $\{\omega_m, \omega_s, \omega_m - \omega_s\} \gg \{|\alpha_0|, |\beta|, |g|\}$ and $\omega_m \gg \omega_s$ are satisfied. The second term on the right hand side represents an artificial radiation pressure interaction analogous to the Pockels effect. On the other hand, the undesired first term corresponds to a self-Kerr nonlinearity, which can be eliminated by finding experimental conditions where α vanishes. As we will show later, this condition could mitigate the saturation effect and provide a full functionality of the realized artificial radiation pressure.

Figure 1e shows the calculated strengths of the self-Kerr nonlinearity α and Pockels nonlinearity β for the parameters of our sample. Notably, α vanishes at certain flux bias conditions $\Phi = \{\Phi_{\alpha=0}, \Phi_0 - \Phi_{\alpha=0}\} \bmod \Phi_0$ (vertical dashed lines in Figs. 1e-g). The second term of the interaction \hat{V}_{eff} has the form of the canonical radiation pressure interaction proportional to β . In canoni-

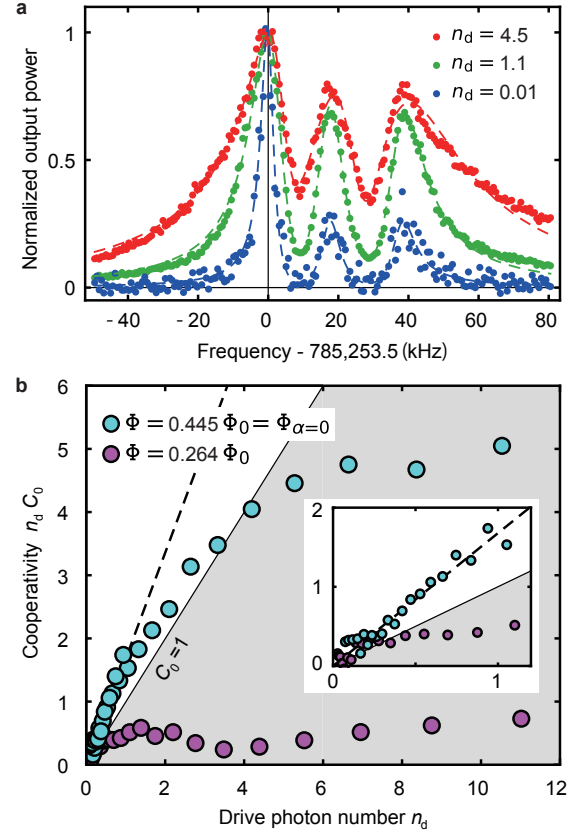


FIG. 3: **Strong artificial radiation pressure.** **a.** Normalized output power of the MW signal coherently up-converted from the SAW excitations as a function of the detuning of the SAW drive frequency (dots). Three datasets are for different drive powers represented by the average number, n_d , of drive photons in the MW resonator. Dashed curves are the results of fittings with a sum of three Lorentzians in the complex plane. The left-most peak is from the fundamental transverse mode of the SAW resonator, while the two other peaks are due to higher-order transverse modes. **b.** Cooperativity $C = n_d C_0$ as a function of the drive photon number n_d . White area corresponds to the single photon quantum regime, i.e., $C_0 > 1$. Cyan dots are the experimental data at $\Phi = 0.445\Phi_0 = \Phi_{\alpha=0}$. Purple dots are taken at $\Phi = 0.264\Phi_0$, where $\alpha \neq 0$ and the saturation takes place at lower power. Black dashed line is the linear fit for the cyan dots in the low-power region. Inset shows the enlarged view near the origin.

cal optomechanical systems, the resonance frequency of the optical (or electrical) resonator is directly affected by the displacement of the mechanical oscillator. Here, in contrast, the resonance frequency of the MW resonator is modulated by the current excited by the mechanical oscillations through the piezoelectric effect, resulting in the Pockels nonlinearity and the synthetic optomechanical coupling. Figure 1f shows the calculated strength g_0 of this artificial radiation pressure interaction. It is of importance that g_0 takes a large value at the flux bias where α vanishes.

Figure 2 shows the experimentally determined nonlinearities as a function of the flux bias. We measure the shift of the MW resonator frequency normalized by the probe photon number as a function of the flux bias. The observed self-Kerr nonlinearity changes its sign near $\Phi = \pm 0.5\Phi_0$, as expected. In the inset of Fig. 2a, the self-Kerr nonlinearity vanishes at $\Phi_{\alpha=0} \equiv 0.445\Phi_0$. The relatively large scattering of the experimental data points are presumably due to the uncertainty in the determination of the probe photon number in the resonator because of the strongly flux-dependent MW resonator loss rates (See Fig. S1 in the Supplementary Information [25]).

To evaluate the strength of Pockels nonlinearity β , we perform a phonon-to-photon conversion experiment from the SAW resonator to the MW resonator. Following the standard optomechanics approach, we linearize the radiation pressure interaction under the red-sideband drive at frequency ω_d . Then the total Hamiltonian at $\Phi = \Phi_{\alpha=0}$ becomes

$$\hat{H} = \Delta \hat{a}^\dagger \hat{a} + \omega_s \hat{b}^\dagger \hat{b} + g_0 \sqrt{n_d} (\hat{a}^\dagger \hat{b} + \hat{a} \hat{b}^\dagger), \quad (7)$$

where n_d is the average photon number of the drive field in the MW resonator and $\Delta \equiv \omega_m - \omega_d$ is the detuning. When the drive field is tuned to the red-sideband transition, i.e., $\Delta = \omega_s$, the two resonators are resonantly coupled to each other. With the red-sideband drive, the excitation of the SAW resonator is converted to the excitation of the MW resonator, and its output MW power P_{out} can be written as

$$P_{\text{out}} = \hbar \omega_m \kappa_{\text{ex}} n_s \frac{4C_0 n_d}{(1 + C_0 n_d)^2}, \quad (8)$$

where $C_0 \equiv 4g_0^2/(\kappa\Gamma)$ is the single-photon cooperativity between the SAW and MW resonators, κ and Γ are the respective total loss rates, and κ_{ex} is the external coupling of the MW resonator. The intra-resonator phonon number n_s of the SAW resonator is calibrated by the Stark shift of the MW resonator (See Fig. S5 in the Supplementary Information [25]). Figure 2b shows the strength of the Pockels nonlinearity β evaluated from the observed conversion efficiency. Here we use a weak drive field which provides a small number of intra-resonator photons ($n_d \sim 0.01$) to avoid saturation of the MW resonator. The overall behavior agrees well with the theoretical prediction.

Finally, we apply a strong red-sideband drive to obtain a large cooperativity with the artificial radiation pressure. This results in the increase of the effective decay rate of the SAW resonator, which is called optomechanical damping. Figure 3a shows the spectra of the SAW resonator in the presence of the optomechanical damping rate Γ_{opt} . The total linewidth Γ_{all} of the spectrum is given by

$$\Gamma_{\text{all}} = \Gamma + \Gamma_{\text{opt}} = (1 + C_0 n_d)\Gamma, \quad (9)$$

from which we evaluate the cooperativity $C = C_0 n_d$.

Figure 3b shows the cooperativity C as a function of the drive photon number n_d at $\Phi = 0.445\Phi_0 = \Phi_{\alpha=0}$ and $\Phi = 0.264\Phi_0$, respectively. Because of the absence of the self-Kerr nonlinearity, the saturation effect is much less pronounced at $\Phi = \Phi_{\alpha=0}$, allowing us to drive the system as in other optomechanical systems with the radiation pressure interaction. The cooperativity reaches 5 at high drive power. The remaining saturation effect is presumably due to the higher-order nonlinearities beyond the third order. The slope of the cooperativity for the small drive photon number corresponds to the single-photon cooperativity C_0 , which is determined to be 1.7 ± 0.1 from the linear fit in Fig. 3. Thus, the single photon quantum regime $C_0 > 1$ is achieved here. From this value, the optomechanical coupling strength is evaluated to be $g_0/2\pi = 190$ kHz, which agrees well with the calculation shown in Fig. 1f. It is also consistent with the estimation of β from the peak power of the up-conversion signal [Eq (6)], which gives $g_0/2\pi = 230$ kHz.

We can straightforwardly improve the system by using a SAW resonator with higher frequency to reduce the detuning from the MW resonator (See Fig. S3b of the Supplementary Information [25]). We can further achieve the condition $g_0/\kappa > 1$, where the presence of a single phonon will shift the resonance frequency of the MW resonator by more than its linewidth [26]. It will then allow for quantum nondemolition measurement of phonon Fock states and thus observation of quantum jumps between them [27].

SAW resonators can also be coupled coherently to an optical system via the opto-elastic interaction [28–30]. Hybrid quantum systems consisting of a SAW resonator and a superconducting qubit open the possibilities of an optical access to a superconducting qubit.

Acknowledgements

The authors acknowledge K. Kusuyama for the help in sample fabrication. This work was partly supported by JSPS KAKENHI (Grant Number 26220601), JST PRESTO (Grant Number JPMJPR1429), and JST ERATO (Grant Number JPMJER1601).

Author contributions

AN fabricated the devices. AN operated the all experiments and analyzed the data. YT and TY managed experimental facilities. YN supervised the project. All author wrote the manuscript.

Method

The parameters in the sample are the following. At zero flux bias, the resonance frequency of the MW resonator is $\omega_m/2\pi = 5.98$ GHz, and the internal and total loss rates are 10 MHz and 55 MHz, respectively. At $\Phi = \Phi_{\alpha=0} \equiv 0.445\Phi_0$, the resonance frequency is 3.85 GHz, the internal loss rate $\kappa_{in}/2\pi = 3$ MHz, and the external loss rate $\kappa_{ex}/2\pi = 17$ MHz. The resonance frequency of the SAW resonator is found to be $\omega_s/2\pi = 785.25$ MHz, together with the total loss rate $\Gamma/2\pi = 4.4$ kHz. The external coupling rate is designed to be $\Gamma_{ex}/2\pi = 0.6$ kHz. The piezoelectric coupling strength evaluated from the frequency shift of the SAW resonator under a strong drive is $g/2\pi = 6.4$ MHz [19]. The strength of the self-Kerr nonlinearity at zero flux bias is determined as $\alpha_0/2\pi = -13.0$ MHz (See the details in the Supplementary Information [25]).

-
- * noguchi@qc.rcast.u-tokyo.ac.jp
- [1] Nichols E. F. and Hull G. F., A Preliminary Communication on the pressure of heat and light radiation, *Phys. Rev.* **13**, 307 (1901).
 - [2] Aspelmeyer M., Kippenberg T. J. and Marquardt F., Cavity optomechanics, *Rev. Mod. Phys.* **86**, 1391 (2014).
 - [3] Teufel J. D., Donner T., Li D., Harlow J. W., Allman M. S., Cicak K., Sirois A. J., Whittaker J. D., Lehnert K. W. and Simmonds R. W., Sideband cooling of micromechanical motion to the quantum ground state, *Nature* **475**, 359 (2011).
 - [4] Lecocq F., Teufel J. D., Aumentado J. and Simmonds R. W., Resolving the vacuum fluctuations of an optomechanical system using an artificial atom, *Nat. Phys.* **11**, 635 (2015).
 - [5] Noguchi A., Yamazaki R., Ataka M., Fujita H., Tabuchi Y., Ishikawa T., Usami K. and Nakamura Y., Ground state cooling of a quantum electromechanical system with a silicon nitride membrane in a 3D loop-gap cavity, *New J. Phys.* **18**, 103036 (2016).
 - [6] Chan J., Alegre T. P. M., Safavi-Naeini A. H., Hill J. T., Krause A., Gröblacher S., Aspelmeyer M. and Painter O., Laser cooling of a nanomechanical oscillator into its quantum ground state, *Nature* **478**, 89 (2011).
 - [7] Hong S., Riedinger R., Marinkovic I., Wallucks A., Hofer S. G., Norte R. A., Aspelmeyer M., Gröblacher S., Hanbury Brown and Twiss interferometry of single phonons from an optomechanical resonator, *Science* **358**, 203 (2017).
 - [8] Purdy T. P., Grutter K. E., Srinivasan K. and Taylor J. M., Quantum correlations from a room-temperature optomechanical cavity, *Science* **356**, 1265 (2017).
 - [9] Frattini N. E., Vool U., Shankar S., Narla A., Sliwa K. M. and Devoret M. H., 3-wave mixing Josephson dipole element, *Appl. Phys. Lett.* **110**, 222603 (2017).
 - [10] Verhagen E., Deléglise S., Weis S., Schliesser A. and Kippenberg T. J., Quantum-coherent coupling of a mechanical oscillator to an optical cavity mode, *Nature* **482**, 63 (2012).
 - [11] Santos J. T., Li J., Ilves J., Ockeloen-Korppi C. F. and Sillanpää M., Optomechanical measurement of a millimeter-sized mechanical oscillator approaching the quantum ground state, *New J. Phys.* **19**, 103014 (2017).
 - [12] Meenehan S. M., Cohen J. D., Gröblacher S., Hill J. T., Safavi-Naeini A. H., Aspelmeyer M. and Painter O., Silicon optomechanical crystal resonator at millikelvin temperatures, *Phys. Rev. A* **90**, 011803(R) (2014).
 - [13] Pirkkalainen J.-M., Cho S. U., Massel F., Tuorila J., Heikkilä T. T., Hakonen P. J. and Sillanpää M. A., Cavity optomechanics mediated by a quantum two-level system, *Nat. Commun.* **6**, 6981 (2015).
 - [14] Gustafsson M. V., Santos P. V., Johansson G. and Delsing P., Local probing of propagating acoustic waves in a gigahertz echo chamber, *Nat. Phys.* **8**, 338 (2012).
 - [15] Manenti R., Peterer M. J., Nersisyan A., Magnusson E. B., Patterson A. and Leek P. J., Surface acoustic wave resonators in the quantum regime, *Phys. Rev. B* **93**, 041411 (2016).
 - [16] Datta S., *Surface Acoustic Wave Devices* (Prentice-Hall, Upper Saddle River, NJ, 1986).
 - [17] Gustafsson M. V., Aref Th., Kockum A. F., Ekstrom M. K., Johansson G. and Delsing P., Propagating phonons coupled to an artificial atom, *Science* **346**, 207 (2014).
 - [18] Manenti R., Kockum A. F., Patterson A., Behrle T., Rahamim J., Tancredi G., Nori F. and Leek P. J., Circuit quantum acoustodynamics with surface acoustic waves, *Nat. Commun.* **8**, 975 (2017).
 - [19] Noguchi A., Yamazaki R., Tabuchi Y. and Nakamura Y., Qubit-assisted transduction for a detection of surface acoustic waves near the quantum limit, *Phys. Rev. Lett.* **119**, 180505 (2017).
 - [20] Satzinger K. J., Zhong Y. P., Chang H.-S., Peairs G. A., Bienfait A., Chou M.-H., Cleland A. Y., Conner C. R., Dumur E., Grebel J., Gutierrez I., November B. H., Povey R. G., Whiteley S. J., Awschalom D. D., Schuster D. I., and Cleland A. N., Quantum control of surface acoustic wave phonons, arXiv:1804.07308 (2018).
 - [21] Chu Y., Kharel P., Yoon T., Frunzio L., Rakich P. T., and Schoelkopf R. J., Climbing the phonon Fock state ladder, arXiv:1804.07426 (2018).
 - [22] Nakamura Y., Pashkin Y. A. and Tsai J. S., Coherent control of macroscopic quantum states in a single-Cooper-pair box, *Nature* **398**, 786 (1999).
 - [23] Wallraff A., Schuster D. I., Blais A., Frunzio L., Huang R.-S., Majer J., Kumar S., Girvin S. M. and Schoelkopf R. J., Strong coupling of a single photon to a superconducting qubit using circuit quantum electrodynamics, *Nature* **431**, 162 (2004).
 - [24] Yamamoto T., Inomata K., Watanabe M., Matsuba K., Miyazaki T., Oliver W. D., Nakamura Y. and Tsai J. S., Flux-driven Josephson parametric amplifier, *Appl. Phys. Lett.* **93**, 042510 (2008).
 - [25] *Supplementary Information*
 - [26] Murch K. W., Moore K. L., Gupta S. and Stamper-Kurn D. M., Observation of quantum-measurement backaction with an ultracold atomic gas, *Nature* **4**, 561 (2008).
 - [27] Miao H., Danilishin S., Corbitt T. and Chen Y., Standard quantum limit for probing mechanical energy quantization, *Phys. Rev. Lett.* **103**, 100402 (2009).
 - [28] Shumeiko V. S., Quantum acousto-optic transducer for superconducting qubits, *Phys. Rev. A* **93**, 023838 (2016).
 - [29] Balram K. C., Davanco M. I., Song J. D. and Srinivasan K., Coherent coupling between radiofrequency, optical and acoustic waves in piezo-optomechanical circuits, *Nat. Photo.* **10**, 346 (2016).
 - [30] Okada A., Oguro F., Noguchi A., Tabuchi Y., Yamazaki R., Usami K. and Nakamura Y., Cavity optomechanics with surface acoustic waves, arXiv:1705.04593 (2017).

Supplementary information

SAMPLE

The circuit was fabricated on a 500- μm -thick ST-X cut quartz substrate. The Bragg mirrors, the interdigitated transducers (IDTs), the nonlinear microwave (MW) resonator, and the coplanar waveguides for the external feed lines were simultaneously patterned in a wet-etching process from a 50-nm-thick evaporated aluminum film. The Bragg mirrors have 750 fingers each. The IDT for the external coupling has a pair of four fingers, and the IDT connected to the MW resonator has a pair of ten fingers (Fig. 1g in the main text). All those fingers have a width and a spacing of 1 μm . The length of the surface-acoustic-wave (SAW) resonator, the inner distance between the Bragg mirrors, is 240 μm . The widths of the Bragg mirrors and the IDTs are 500 μm . The Josephson junctions for the SNAIL are made from Al/AIO_x/Al junctions, which are simultaneously fabricated by the shadow evaporation technique with the bridgeless resist mask. The size of the junctions are 150 \times 150 nm for the small one and 300 \times 300 nm for the large ones.

Figure S1 shows the resonance frequency and the loss rates of the MW resonator as a function of the magnetic flux in the SNAIL loop. Note that the loss rates are periodically fluctuating depending on the flux bias. The periodic modulation is presumably caused by the resonant acoustic radiation from the MW resonator. The internal loss rate κ_{in} is divided into the electric loss κ_e and the acoustic radiation loss κ_a from the MW resonator. The part of the acoustic radiation is picked up by the IDT electrode of the SAW resonator, and thus $\kappa_a = \kappa_{\text{cross}} + \kappa_{\text{rad}}$, where κ_{cross} is the external coupling rate of the MW resonator through acoustic waves to the SAW input port (port 3 in Fig. 1a) and κ_{rad} is the acoustic radiation rate to the environment. Figure S1d shows the acoustic external coupling rate κ_{cross} of the MW resonator to the SAW input port (port 3 in Fig. 1a).

NONLINEAR RESONATOR WITH SNAIL

Our SNAIL has a single small junction and two large junctions. It is shunted with a large capacitor whose single-electron charging energy E_C is estimated to be $h \times 35$ MHz. To determine the Josephson energies in the device, we fit the flux-dependent spectrum in Fig. 1g and obtain $E_J' = h \times 47.5$ GHz and $E_J = h \times 163.5$ GHz, respectively. Figure S2 shows the inductive energy $U(\theta)$ of the SNAIL, given by Eq.(1) in the main text, in units E_J . For $\Phi \neq 0$, the parity symmetry is broken and the Pockels nonlinearity appears. The inductive energy is expanded around the minimum at θ_0 in a power series of

$\tilde{\theta} \equiv \theta - \theta_0$ as

$$U(\tilde{\theta})/E_J = -\sum \chi_i \tilde{\theta}^i. \quad (\text{S1})$$

The Hamiltonian of this nonlinear resonator in the transmon limit ($E_J \gg E_C$) reads

$$\hat{H} = 4E_C \hat{N}^2 - E_J \sum \chi_i \hat{\theta}^i, \quad (\text{S2})$$

where \hat{N} is the number operator of the superconducting electrode connected to the ground via the SNAIL. For the phase operator $\hat{\theta}$, we omit the tilde for simplicity. This Hamiltonian can be rewritten with the creation and annihilation operators as

$$\begin{aligned} \hat{H} = & \left(\sqrt{16E_C E_J \chi_2} - 12E_C \frac{\chi_4}{\chi_2} \right) \hat{a}^\dagger \hat{a} \\ & - 3E_C \left(\frac{\chi_2 E_J}{E_C} \right)^{1/4} \frac{\chi_3}{\chi_2} (\hat{a}^\dagger \hat{a}^\dagger \hat{a} + \text{h.c.}) \\ & - 6E_C \frac{\chi_4}{\chi_2} \hat{a}^\dagger \hat{a}^\dagger \hat{a} \hat{a} + O(\hat{a}^5), \end{aligned} \quad (\text{S3})$$

where

$$\hat{a} = \left(\frac{E_C}{h^2 \chi_2 E_J} \right)^{1/4} \left(i\hat{N} + \sqrt{\frac{\chi_2 E_J}{4E_C}} \hat{\theta} \right). \quad (\text{S4})$$

The Pockels (second-order) and self-Kerr (third-order) nonlinearities appear in Eq.(S3). This relates the circuit parameters to the coefficients of the nonlinear terms.

ARTIFICIAL OPTOMECHANICAL COUPLING

The total Hamiltonian of the hybrid system consisting of a nonlinear MW resonator and a SAW resonator piezoelectrically coupled to each other is described without rotating wave approximation as

$$\hat{H} = \hat{H}_0 + \hat{V}_0, \quad (\text{S5})$$

where

$$\hat{H}_0 = \omega_m \hat{a}^\dagger \hat{a} + \omega_s \hat{b}^\dagger \hat{b}, \quad (\text{S6})$$

and

$$\begin{aligned} \hat{V}_0 = & \beta (\hat{a}^\dagger \hat{a}^\dagger \hat{a} + \text{h.c.}) + \alpha_0 \hat{a}^\dagger \hat{a}^\dagger \hat{a} \hat{a}, \\ & + g (\hat{a}^\dagger + \hat{a}) (\hat{b}^\dagger + \hat{b}). \end{aligned} \quad (\text{S7})$$

The parameters and the operators are defined in the main text.

By treating \hat{V}_0 as a perturbation, we find the effective

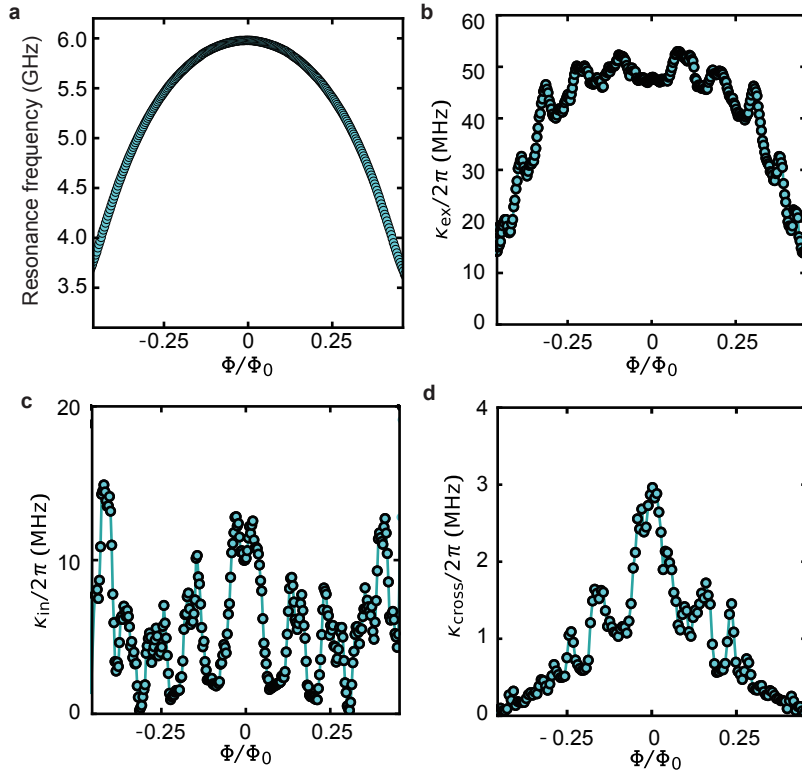


FIG. S1: Parameters of the nonlinear MW resonator as a function of the flux bias. **a.** The resonance frequency $\omega_m/2\pi$, **b.** external loss rate κ_{ex} , **c.** internal loss rate κ_{in} and **d.** acoustic external loss rate to the IDT electrode are evaluated from the spectroscopy at the low-power limit with input-output theory.

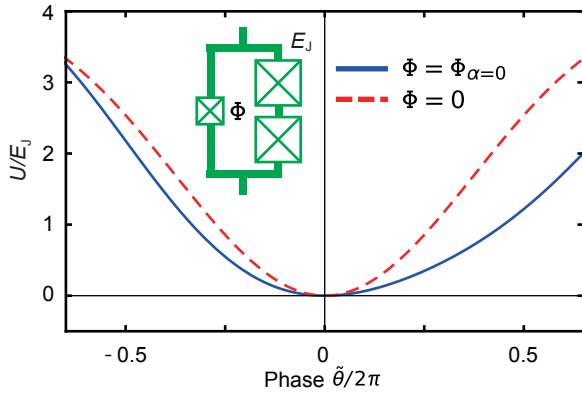


FIG. S2: Inductive energy $U(\tilde{\theta})$ of the SNAIL as a function of the phase difference $\tilde{\theta}$ across the small Josephson junction. The inset shows the circuit model of the SNAIL.

Hamiltonian as

$$\begin{aligned}
 \hat{H}_{\text{eff}} = & \hat{H}_0 + \left(\alpha_0 - \frac{3\beta^2}{\omega_m} \right) \hat{a}^\dagger \hat{a}^\dagger \hat{a} \hat{a} \\
 & - \left(\frac{g\beta}{\delta} + \frac{g\beta}{\omega_m} \right) \hat{a}^\dagger \hat{a} (\hat{b}^\dagger + \hat{b}) \\
 & - \frac{g\beta\omega_s}{2\omega_m\delta} (\hat{a}^\dagger \hat{a}^\dagger \hat{b} + \text{h.c.}) \\
 & + \frac{g\beta\omega_s}{2\omega_m(\omega_m + \omega_s)} (\hat{a}^\dagger \hat{a}^\dagger \hat{b}^\dagger + \text{h.c.}) \\
 & - \frac{2g\alpha_0}{\omega_m + \omega_2} (\hat{a}^\dagger \hat{a} \hat{a} \hat{b} + \text{h.c.}) \\
 & - \frac{2g\alpha_0}{\omega_m - \omega_2} (\hat{a}^\dagger \hat{a} \hat{a} \hat{b}^\dagger + \text{h.c.}) \\
 & - \frac{2\alpha_0\beta}{\omega_m} (\hat{a}^\dagger \hat{a}^\dagger \hat{a} \hat{a} + \text{h.c.}), \tag{S8}
 \end{aligned}$$

where $\delta = \omega_m - \omega_s$ is the detuning between the MW and SAW resonators. This calculation is valid when $\{\omega_m, \omega_s, \delta\} \gg \{|\alpha_0|, |\beta|, |g|\}$ is satisfied. While the second term on the right-hand side gives the self-Kerr nonlinearity, the third term leads to the radiation pressure interaction, and the fourth term introduces Casimir effect. When $\alpha_0 = 3\beta^2/\omega_m$, the self-Kerr nonlinearity

vanishes, and the effective Hamiltonian is rewritten as

$$\hat{H}_{\text{eff}} = \hat{H}_0 - 2\frac{g\beta}{\delta}\hat{a}^\dagger\hat{a}(\hat{b}^\dagger + \hat{b}), \quad (\text{S9})$$

with the rotating wave approximation and the large detuning ($\delta \sim \omega_m$).

Figures S3a and S3b show the optomechanical coupling strength g_0 and the resulting single photon cooperativity C_0 , calculated based on the parameters in the present device. In Fig. S3a, we sweep the Josephson energy E_J of the large junctions in the SNAIL. Both g_0 and C_0 increase as E_J decreases and the nonlinearity increases. Note that, however, when the Josephson energy of the large junctions is smaller than twice of that of the small junction, i.e., $E_J/E'_J \leq 2$, the potential landscape of the inductive energy of the SNAIL has multiple wells, and the capacitively shunted SNAIL behaves like a flux qubit. In Fig. S3b, we look at the dependence on the SAW resonance frequency $\omega_s/2\pi$. As the SAW resonance frequency approaches that of the MW resonator, the optomechanical coupling strength g_0 becomes larger. Simultaneously, the small mode volume of the high-frequency SAW resonator enhances the coupling strength.

SELF-KERR NONLINEARITY

We characterize the amount of the self-Kerr nonlinearity of the MW resonator by measuring the frequency shift as a function of the probe power. Figures S4a and S4b show the frequency shift and the saturation of the absorption in the MW resonator at zero flux bias, respectively. To analyze the result, we solve the master equation of the resonator with the third-order nonlinearity and fit the experimental data. In the steady state, it fulfills

$$i[\hat{\rho}, \hat{H}_{\text{fit}}] + \hat{L}[\hat{\rho}] = \dot{\hat{\rho}} = 0, \quad (\text{S10})$$

where $\hat{\rho}$ is the density operator of the MW resonator, \hat{L} is the Lindblad superoperator, and

$$\begin{aligned} \hat{H}_{\text{fit}} = & \sqrt{4A_m P_m \kappa_{\text{ex}} / \hbar \omega_m} (\hat{a}^\dagger + \hat{a}) \\ & + \Delta \hat{a}^\dagger \hat{a} + \alpha \hat{a}^\dagger \hat{a}^\dagger \hat{a} \hat{a}. \end{aligned} \quad (\text{S11})$$

Here, A_m is the attenuation through the input line of the MW feedline, and P_m is the probe power at the input port outside the refrigerator. The saturation effect is highly nonlinear so that we can calibrate the absolute internal photon number with respect to the applied MW power. The strength of the self-Kerr nonlinearity and the attenuation in the input lines are determined from the fits as $\alpha/2\pi = \alpha_0/2\pi = -13.0$ MHz and -57.3 dB, respectively.

STARK SHIFT BY THE SAW EXCITATION

To calibrate the SAW input power, we measure the Stark shift of the MW resonator induced by the SAW excitation. Figure S5 shows the Stark shift as a function of the phonon number in the SAW resonator at zero flux bias. Here we use the Stark shift per single phonon which is calculated to be

$$\chi_s = \frac{2g^2\alpha_0}{\delta^2} = 2\pi \times 22 \text{ Hz}. \quad (\text{S12})$$

The intra-resonator phonon number of the SAW resonator is given as $n_s = 4A_s P_s / \hbar \omega_s \Gamma$, where P_s is the drive power at the SAW input port outside the refrigerator. From comparison with the experimental result, the attenuation A_s along the SAW input line is determined to be -73 dB including the effect of the external coupling efficiency of the SAW resonator.

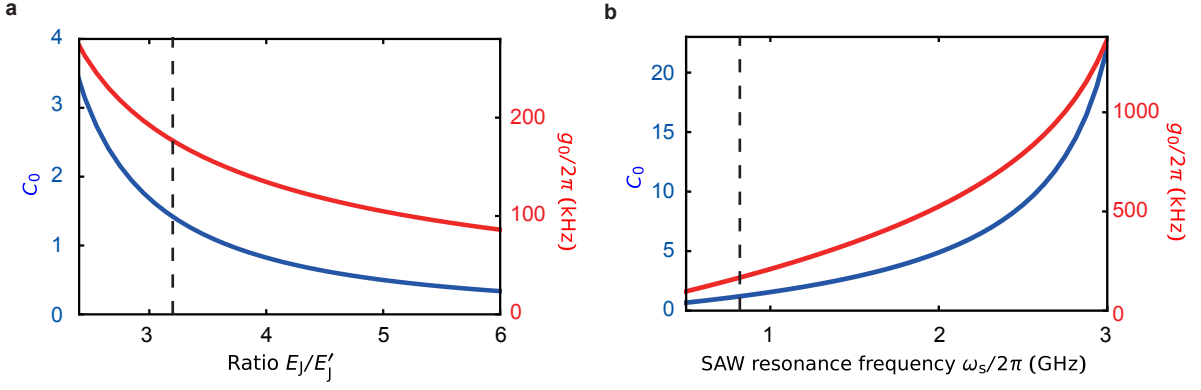


FIG. S3: Estimation of the optomechanical coupling strength. Blue and red curves show the single photon cooperativity C_0 and the strength of the single photon radiation pressure interaction g_0 , respectively. The Josephson energy E_J of the larger junctions in the SNAIL and the SAW resonator frequency $\omega_s/2\pi$ are swept in **a** and **b**, respectively. Vertical dashed lines indicate the parameters in the current experiment. Other parameters are set to the values obtained in the experiment.

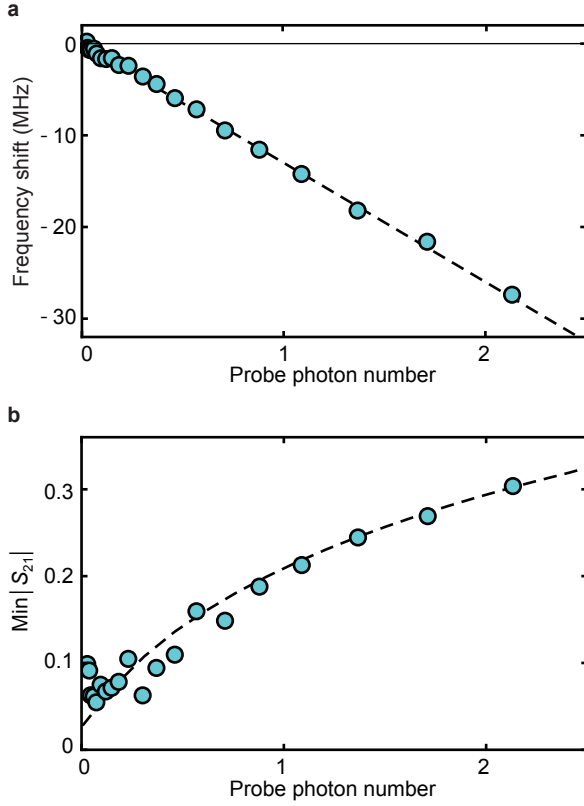


FIG. S4: Calibration of the resonator photon number and the nonlinearity of the MW resonator. **a**. Frequency shift of the nonlinear MW resonator as a function of the probe power represented by the intra-resonator photon number. **b**. Saturation of the nonlinear MW resonator as a function of the probe power. The vertical axis shows the minimum values of the normalized transmission coefficient $|S_{21}|$ at the resonance of the MW resonator. The Self-Kerr nonlinearity makes the MW resonator saturated.

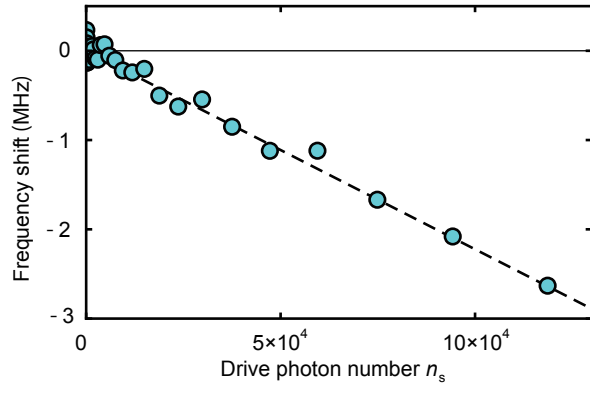


FIG. S5: Stark shift of the MW resonator due to the excitation of phonons in the SAW resonator.